Morphological and functional alteration of light perception circuits in AD patients

Nicolae Sanda (1)(2), Dan Milea (3)(4), Eniko Kovari (5), Yixin Tong (6)(7), Talayeh Brügger (8), Jens Hannibal (9), Kristof Levente Egervari (10), Johannes Alexander Lobrinus (10), Emmanuel Carrera (2)(11), Gabriele Thumann (2)(12), Sonja Kleinlogel (8)(13), Antoine Adamantidis (7)(14), Ludovic S. Mure (6)(7)(14)*

Affiliations

(1) Fribourg Cantonal Hospital, Neurology Department, Fribourg, Switzerland

(2) Department of Clinical Neurosciences, Geneva University, Geneva, Switzerland

(3) Rothschild Foundation Hospital, Neuro-ophthalmology Department, Paris, France

(4) Singapore National Eye Centre, Singapore and Duke-NUS Medical School, Singapore

(5) Faculty of medicine, University of Geneva, Switzerland

(6) Inselspital, Department of Ophthalmology, Bern, Switzerland

(7) University of Bern, DBMR, Bern, Switzerland

(8) University of Bern, Institute of Physiology, Bern, Switzerland

(9) Department of Clinical Biochemistry, Bispebjerg Hospital, Department of Clinical Medicine, Faculty of Health and Medical Sciences, University of Copenhagen, Copenhagen, Denmark

(10) Geneva University Hospital, Neuropathology Unit, Geneva, Switzerland

(11) Geneva University Hospital, Stroke Center, Geneva, Switzerland

(12) Geneva University Hospital, Ophthalmology Department, Geneva, Switzerland

(13) current address: F. Hoffmann-La Roche Ltd, Translational Medicine Neuroscience, Basel, Switzerland

(14) Inselspital, Zentrum für Experimentelle Neurologie, Department of Neurology, Bern, Switzerland.

*correspondence: ludovic.mure@unibe.ch

Liste of abbreviations

p-tau hyperphosphorylated tau

Aβ amyloid beta

NFT neurofibrillary tangles

SP senile plaques

POA preoptic area

SCN suprachiasmatic nucleus

ACC accumbens nucleus

AMY amygdala central nucleus

LGN lateral geniculate nucleus

LHB/pLHB lateral habenula/peri lateral habenula

SC superior colliculus

EWN Edinger-Westphal nucleus

LDT laterodorsal tegmental nucleus

PPT pedunculopontine tegmental nucleus

LC locus coeruleus

PBN parabrachial nucleus

VC primary visual cortex

Abstract

Disruption of sleep and circadian rhythms is one of the earliest symptoms of Alzheimer's disease (AD). Circadian entrainment and the modulation of alertness are non-visual responses to light driven by intrinsically photosensitive retinal ganglion cells (ipRGCs). However, little is known about ipRGCs in the context of AD. To explore structural and functional changes of ipRGCs and ipRGC circuits, we analyzed the retinas and brains of 13 elderly patients (9 males, 4 females, aged 69-103) ranging from normal to neuropathologically defined AD.

We performed extracellular electrophysiological recordings on freshly harvested retinas using multi-electrode arrays. While rod and cone responses were moderately affected, we found a decreased density of ipRGCs in donors with advanced AD pathology, which was confirmed by immunostaining. The remaining ipRGCs displayed morphological alterations as well as abnormal responses to light, including hyperexcitability. These changes appeared to be subtype-specific and correlated with the advancement of the disease.

Altered ipRGCs circuits and function could contribute to the disruption of sleep and circadian rhythms reported in AD patients. The measurement of ipRGC-dependent responses to light could constitute a promising tool to predict or monitor pathological changes in the brain.

Introduction

Alzheimer's disease (AD) is a devastating neurodegenerative disorder and the most common cause of dementia. characterized by progressive cognitive decline, memory loss, and impaired daily functioning(*1*). AD neuropathological features, such as the presence of amyloid-beta plaques and tau protein containing tangles, play a central role in the disease progression. A definitive and unambiguous diagnosis is difficult to establish, and by the time it is obtained, the disease has usually progressed over decades, causing significant neurodegeneration. Dementia is estimated to affect more than 55 million patients, however its prevalence continues to rise with the aging of the population, and it's projected to double by 2050(*2*).Understanding the underlying disease mechanisms and identifying potential early biomarkers is urgently needed to allow timely diagnosis and intervention.

One of the earliest symptoms in AD is a disruption of sleep and circadian rhythms. Individuals with Alzheimer's often experience increasingly fragmented sleep and altered core body temperature rhythm(*3–6*). There is now abundant evidence that disruption of the daily rhythms can occur years before the emergence of classical symptoms, such as memory loss in AD(*7*, *8*). Excessive daytime sleepiness and sleep behavior disorders are associated with an increased risk of developing AD and dementia suggesting that dysregulation of sleep may be important in the early pathogenesis of neurodegeneration(*9–12*). These behavioral disruptions not only compromise the quality of life of the patient, but they cause physical and psychological fatigue in the caregiver and are often the reason for institutional placement.

Regulation of non-visual responses to light including synchronizing the circadian clock to the day-night cycle and regulating sleep, alertness, mood, and the pupillary light reflex (PLR) is mainly mediated by a class of intrinsically photosensitive retinal ganglion cells (ipRGCs) that express the light-sensing protein melanopsin. Accordingly, when ipRGCs are selectively ablated or when signaling properties of melanopsin are changed, photoentrainment of the clock, acute light-modulation of sleep, and PLR to light are abolished or maladapted(*13–16*). Interestingly, a recent histological study has shown a specific decline in ipRGCs number in the retina of AD patients(*17*). Beta amyloid accumulation was also observed inside and around ipRGCs suggesting that the response properties of ipRGCs from AD patients may be altered(*17*). In mouse models of AD, ipRGC anomalies have also been reported(*18*, *19*). While these observations suggest that light

97 perception circuits may be damaged in Alzheimer's disease, this has never been investigated
98 further in patients.
99 The aim of this study was to evaluate the alteration of light perception in AD patients
100 compared to normal individuals, using a comprehensive exploration in eye-brain donors.
101 Specifically, we investigated the histological and functional changes in ipRGC circuits in the retina
102 and brain of patients at different stages of Alzheimer's disease.
103
104 **Results**
105 To assess the impact of AD on light perception, we conducted an exploratory, multi-angle
106 study on 13 eye and brain donors, deceased at the Geneva Stroke Center (Geneva, Switzerland,
107 **FigS1A**). The demographic characteristics of the cohort are presented in **Table 1**. Age ranged from
108 69 to 103 years (81.31 ± 3.011). There were 9 males (mean age 79.44 ± 3.17 years; 69 to 97 years)
109 and 4 females (mean age 85.50 ± 7.01 y ears; 70 to 103 years, p=0.49, Mann Whitney test). The
110 cause of death was brain infarct and/or brain hemorrhage (**Table1**). Among the included donors,
111 two showed ante-mortem signs of dementia (donors 3 and 5), which together with their post-
112 mortem neuropathology support a diagnosis of Alzheimer's disease and are therefore referred to in
113 this manuscript as AD donors, as opposed to donors without known cognitive impairments (ND,
114 non-demented, donors). The neuropathological severity of tau lesions and amyloid deposition were
115 assessed in the anterior hippocampus, entorhinal, transentorhinal, and inferior temporal cortices
116 using the Braak staging for neurofibrillary tangles (NFT) and the Thal phases for senile plaques
117 (SP) (**FigS1B-D)**(*20*, *21*). Thal phases ranged from 0 to 4 and Braak scores ranged from I to VI.
118 The two AD patients scored 3 and 4 and V and VI respectively **(Table1**). Neither Thal phases nor
119 Braak stages were correlated with the age of the donors (**FigS1E**).
120 To quantify AD hallmarks along some of the brain circuits implicated in the regulation of
121 visual and non-visual responses to light, we also examined tau pathology and amyloid deposition
122 in 13 brain regions implicated in vision (LGN, SC, Visual cortex), circadian rhythms (SCN),
123 alertness and sleep regulation (POA, pons nuclei), mood (AMY, LHB/pLHB, ACC), and pupillary
124 reflex to light (EWN) in 13 donors (**Fig1A**). Uniform brain sampling was performed by a
125 neuropathologist and SP and NFT were scored on a 0 to 3 scale by trained pathologists (0=none,
126 1=sparse, 2=moderate, 3=abundant) (**Fig1B**). We found aggregates in the majority of the regions
127 examined. While deposits of Amyloid beta (Aβ) were more abundant as the amyloid pathology

128 progresses, hyperphosphorylated tau (p-tau) burden did not follow this pattern and its presence in
129 light perception circuits appeared uncorrelated with Braak stages (**Fig1C, FigS2A**). Aβ burden in
130 the VC and Acc as well as in all retino-recipient nuclei at the exception of the LGN correlated with
131 the Thal phase of the respective donor (**Fig1C**).

132 To evaluate the correlation between the brain and retina pathologies, we performed
133 immunostaining of Aβ and Tau in the retina of the donors. We manually segmented the outer retina
134 (OR: photoreceptor (PR) and outer plexiform layers (OPL)) and inner retina (IR: inner nuclear
135 (INL), inner plexiform (IPL), and retinal ganglion cell (RGC) layers) (**Fig1D**) and determined the
136 layer distribution of p-tau and Aβ burdens in retinal cross sections. Representative microscopic
137 images show an accumulation of p-tau in patients that correlates with the Braak stage (**Fig1E**).
138 Immunostaining of p-tau revealed diffuse staining in the OPL and intense staining in the INL and
139 IPL including probable intracellular staining in the INL. Aβ deposits were identified in the inner
140 retina, in particular in the innermost RGC and retinal nerve fiber layers. Aβ42 burden (**Fig1E,**
141 **FigS2B**) also increases, although not significantly, with the Thal phase of the donor. Finally, we
142 also measured the thickness of the segmented IR and OR as a proxy of neurodegeneration. The
143 thickness of both layers decreased with AD and was negatively correlated with the increase of
144 Thal phases and Braak stages (**Fig1F**).

145 The presence in the retina of both Aβ and Tau aggregates and degeneration (**Fig1**)
146 suggested a possible alteration of the light information sent to the brain. To evaluate the function
147 of the rods, cones, and ipRGCs, we recorded responses to light from a donor's retina preparation
148 using multi-electrode array (MEA)(*22*, *23*). Briefly, the eyes of the donors were collected within
149 2 hour postmortem (**Table1**), immediately preserved in oxygenated Ames 'medium placed in a
150 light-proof container, transported to the lab where circular (3mm diameter) patches of retina were
151 dissected under dim red light, placed on MEA, and allowed to recover in darkness for at least
152 1hour.

153 First, to evaluate photoreceptors' function, we recorded micro-electroretinogram
154 (mERG)(*24*) on retinal patches from 5 donors (**Table 1**), including the two AD donors in response
155 to sequences of 10ms light flashes of increasing irradiance (470nm, 6.10^9 to 2.10^{13} photons/cm^2/s)
156 (**FigS3**)**.** mERG did not display major differences in response profiles between AD and age-
157 matched control donors (**FigS3A**). A-waves were detected in all donors at all light irradiances used
158 while b-waves were only clearly detected at the highest light stimulation but in all donors too(*23*).

159 While the amplitude of the a-wave from the AD donors was the smallest, it was not different from
160 that of the other donors. Similarly, the b wave amplitude and the latencies of both waves did not
161 differ between donors (**FigS3B, C**).

162 Then, to evaluate ipRGCs'function, we performed extracellular electrophysiological
163 recordings of freshly harvested retina from 6 donors including the two AD donors (**Table 1**). For
164 this purpose, the recording medium was supplemented with synaptic blockers to block rod and
165 cone input to RGCs and capture ipRGCs intrinsic, melanopsin-initiated signal. In response to 30-
166 s pulses of monochromatic blue light (470 nm), photoresponsive cells were found in retinas from
167 each of the six donors (**Fig2A**). However, the number of ipRGCs varied from one donor to the
168 other. For each retina sample, we identified photoresponsive cells at an average density ranging
169 from <1 to ~8 cells/mm^2 (**Fig2B**). The number of light responsive cells was negatively correlated
170 with the Braak stage but not with the Thal phase, the age of the donor, or the delay of collection
171 of the eye (**Fig2B and FigS4A**). Grouped analysis reveals a two-time decrease in ipRGCs density
172 in retina pieces from AD donors (**FigS4B**).

173 To confirm the ipRGC loss in AD patients, we performed immunostaining against
174 melanopsin as previously described(*25*) and we counted melanopsin positive (mel+) cells in 3mm
175 diameter retina patches (**Fig2C**). We found about two time-decreased density of mel+ in the retina
176 of AD donors (**FigS4B**). When examined individually, mel+ density correlated with the patient
177 Braak stage and ipRGCs density but not with the Thal phase (**Fig2D, E and FigS4C**). Melanopsin
178 staining revealed that not only the number but also the morphology of mel+ cells is affected by the
179 disease. In each retina sample, a blind investigator used semi-automated tracing to reconstruct the
180 dendritic arborization of 4 mel+ cells per retina sample (**Fig2F**). Scholl analysis revealed that while
181 the extend radius of the ipRGCs dendritic tree was not different between donors, its number of
182 intersections midway between the soma and the extremities was decreased in AD donors (**Fig2G,**
183 **FigS4D**). Accordingly, both total neurites length and the number of terminal branches were lower
184 in the AD patients (**Fig2H-I, FigS4D**). These results suggest a decrease in dendritic tree
185 complexity in AD. Interestingly, AD ipRGCs had larger soma (**Fig2J, FigS4D**). Altogether, these
186 major morphological alterations strongly suggest that the function of the surviving ipRGCs is also
187 altered.

188 To evaluate potential functional alteration in the remaining ipRGCs from AD donors, we
189 characterized their response properties. We stimulated the retinas for 30 s at increasing irradiances

190 of monochromatic blue light (470 nm, 2.10^{12} to 1.10^{15} photons/cm^2/s). Overall, responses to light
191 were slow, sustained, and outlasted the stimulus by several seconds after the light was switched
192 off, the sensitivity was low as previously described (*22*) (**Fig2A**). Response properties followed
193 similar dynamics with increasing stimulation irradiance; latency decreased while the duration and
194 number of spikes of the response increased (**Fig3A**). Interestingly, responses to the lowest intensity
195 of light were correlated with the Thal and Braak scores reflecting an increased sensitivity or
196 excitability with the progression of the disease (**Fig3B,C and FigS4E**). Conversely, responses to
197 the highest intensity of light were inversely correlated with the Thal and Braak scores suggesting
198 a failure to sustain responses at advanced stages of AD (**Fig3B,C**).
199 Several morphological and functional ipRGC subtypes have been described in the human
200 retina (*22*, *25–28*). To assess whether the alterations reported above reflect alteration and/or
201 degeneration of specific subtype(s), we performed principal components analysis (PCA) on the
202 response parameters of each ipRGCs recorded. Data separated in at least three main clusters
203 (**Fig3D**) whose response to light properties and time course closely resemble those from previously
204 described ipRGC subtypes (**Fig3D,E**) (*22*). The three subtypes were found in all donors (**Fig3E**)
205 but their distribution was changed in the AD donors. Type1 accounted for half of the ipRGCs in
206 AD donors while type 2 and 3 ipRGCs fraction was strongly decreased (**Fig3F**). When examined
207 individually, type1 fraction correlates with the Braak stage of the donor (**FigS4F**). This result
208 suggests that type 1 cells may be more resilient than type 2 and 3. As type1 ipRGCs are the subtype
209 that is most sensitive to light, the increased excitability observed could be due to this change of
210 distribution. To test this hypothesis, we examined the sensitivity to light of each subtype. We found
211 that type1 ipRGC sensitivity was increased in AD donors (**Fig3G**). Overall, all ipRGC subtypes
212 are affected and the increased excitability observed in AD may rely on both a shift in subtypes
213 distribution toward M1, the most sensitive ipRGCs, and an increase in their sensitivity.
214
215 **Discussion**
216 In this prospective study, we examined several circuits of light perception in a group of
217 elderly adult donors at various stages of AD pathological changes. We employed a comprehensive
218 suite of measurements to compose the first picture of how AD may impact ipRGCs abundance,
219 function, and brain targets and found that ipRGC circuits are injured both morphologically and
220 functionally in the brain and the retina.

221 In the retina, our results are in agreement with the presence and distribution of AD
222 hallmarks and their correlation with the neuropathological changes observed in the brain, reported
223 early and in extensive postmortem retinal histological studies ((*29–33*)(for review see(*34*)). We
224 also confirmed the loss of ipRGCs observed in AD patients(*17*). We extended these findings by
225 measuring *ex vivo* the function of the different photoreceptors. Both outer and inner retina
226 photoreceptors seem to malfunction with AD but, while rods/cones response alteration may be
227 limited to small decrease in amplitude at specific light intensity levels, ipRGCs injury is massive.
228 AD has been associated with various forms of visual dysfunction including abnormal visual
229 fields, reduced color and contrast vision which can be, at least in part, attributed to retinal and
230 optic nerve damage(*35–38*). Retinal abnormalities can be identified with electroretinogram (ERG)
231 in AD (*39–43*). Here, while we found a decrease in IR thickness, the mERG a and b waves did not
232 show significant differences between AD and ND patients in response to our stimulation protocol.
233 Because IR photoreceptor function declines rapidly with hypoxia (*23*), some differences between
234 donors may have been masked by the postmortem functional decline in all donors.
235 ipRGCs are the main contributors and in some cases the exclusive conduits of light
236 regulation to non-visual light responses (*13*, *14*). Accordingly, they project to more than a dozen
237 of brain regions implicated in visual and non-visual responses to light including the nuclei
238 investigated here, SCN, POA, HB/pHb, AMY, LGN, and SC(*44*, *45*). We found twice less ipRGCs
239 in AD donors, and the surviving one displayed abnormal morphologies and responses to light that
240 may precede degeneration. In particular, the increase in soma size resembles the phenomenon
241 called neuronal ballooning that is thought to result from deficient axonal trafficking and
242 subsequent accumulation of cargos at the initial segment (*46–48*). Then, the increased excitability
243 is reminiscent of cerebral neurons in which an increased excitability is observable at the earlier
244 stages of the disease before there is pronounced cell loss and hypoactivity(*49–51*). The initial loss
245 of ipRGCs seems biased toward types 2 and 3, with type 1 ipRGC appear more resilient. M1
246 ipRGCs, the morphological equivalent of functional type1 ipRGCs, had already been shown to
247 demonstrate increased survival to mechanical and metabolic stresses(*52*). However, the
248 morphological and functional alterations observed in AD donor remaining ipRGCs suggest that
249 type1 ipRGCs probably also degenerate. Overall, these alterations are consistent with and could
250 contribute to the alterations of ipRGC-regulated functions, such as circadian rhythm,
251 sleep/alertness, and mood, experienced by AD patients. These results also suggest that some

252 ipRGC-dependent responses to light may be impacted earlier than others and could constitute stage
253 specific markers.

254 As PLR is thought to rely on both M1 and M2 ipRGCs(*53*), our results predict that pupillary
255 responses to light should also be affected. Pupillometry is a scalable, cost effective, non-invasive
256 assay that a few groups have started to explore as a biomarker of AD in pre-symptomatic cases
257 (*54*, *55*) and early AD cases (*56*, *57*). However, the results have been mixed. This may reflect the
258 diversity of light stimuli and protocols (*58*, *59*) and emphasizes the need to determine the spectral,
259 intensity, and/or temporal domains where ipRGCs malfunction and PLR is impacted. For example,
260 our results suggest that injured ipRGCs will fail to sustain response to long stimulations at high
261 irradiance.

262 The retina, an extension of the central nervous system, offers a unique opportunity to study
263 AD pathology outside of the brain. Over the past decades, accumulating evidence has shed light
264 on the presence of AD-related histological changes in the retina, suggesting the potential of
265 different retinal imaging modalities as a non-invasive method to detect and study the disease (for
266 review see(*34*)). Our results suggest that the retinal functions (light perception and transmission to
267 the brain) are also altered and add ipRGC-dependent responses to light as potential biomarkers of
268 AD. In AD donors, surviving ipRGCs seems to recapitulate several phenotypes observed in brain
269 neurons: hyperexcitability and ballooning. This, together with the fact that they are more accessible
270 and have clear cellular and behavioral readouts, makes ipRGC a promising model to study the
271 mechanisms of neuronal degeneration directly in human. Elucidating the mechanisms underlying
272 ipRGC vulnerability to AD could lead to the discovery of therapeutic targets to improve patients'
273 quality of life and potentially improve the overall disease trajectory.

274

275 **Limitations**

276 Our study has a number of limitations. First, our sample size is small because of the
277 challenges presented to obtain and collect postmortem eye and brain tissues from well-
278 characterized participants meeting the criteria of inclusion. However, we partially compensated
279 for this limitation by using in-depth objective physiopathological and functional measurements
280 from each donor. Second, our cohort has a greater proportion of male subjects, leading to potential
281 sex-related bias. Our study population was composed primarily of self-reported White and thus
282 may not be representative of other populations. Third, because our focus was on physiology, the

pieces of retina were collected in the same central region irrespective of the orientation. While this strategy may have caused some variability and may leave apart more extreme phenotypes in the peripheral retina(*17*, *29*, *60*, *61*), ipRGC density and distribution is relatively homogenous in this region(*25*). Finally, our study is primarily correlational and, therefore, caution must be taken before making cause-and-effect inferences.

Despite these limitations, the present study gives a glimpse of pathophysiological mechanisms of neurodegeneration at work in humans.

Data availability

Code and data used to generate the figures described in this paper will be made available via Zenodo (Zenodo.org) at the time of publication, with a DOI to be included here.

Acknowledgements

We thank Dr. G. Benegiamo for critical comments on the manuscript. This study was supported by the Velux Stiftung grant to SK and LSM, the Novartis Biomedical Research Foundation, and the Chan Zuckerberg Initiative grants to AA and LSM. JH is supported from the Danish Center for Cellular Communication.

Contributions

NS, DM, and LSM conceptualized the study. NS and LSM designed it. NS coordinated tissue collections and harvests. NS, EK, YT, TAZ, KLE, and LSM performed the experiments. JH provided the melanopsin antibodies. EK, JH, JAL, EC, GT, SK, and AA provided scientific expertise and critical reading of the manuscript. LSM analyzed the data. LSM wrote the first draft, all authors edited and approved the manuscript.

Competing interests

DM is an advisory board member for Optomed, Finland. All other authors declare that they have no competing interest.

Methods

Donors

314 Patients were prospectively included in the study after obtention of informed consent from the
315 family or healthcare proxys. At a second phase, following the confirmation of death, the patient
316 was promptly transported to the hospital morgue where enucleation was immediately performed,
317 day or night, by a trained physician (NS). Only patients in whom enucleation was performed within
318 2 hours after death were included in the study.
319
320 *Eye sampling procedure*
321 Bilateral enucleation was performed in all eligible patients following a standard surgical
322 procedure. After insertion of a lid speculum, a conjunctival peritomy was performed using a #15
323 blade, followed by dissection of Tenon's capsule. The extraocular muscles were identified,
324 isolated, and transected, facilitating identification and isolation of the optic nerve from the
325 surrounding structures. Using microscissors, the optic nerve was then sharply transsected, as far
326 as possible from its bulbar insertion to the ocular globe, closest possible to the orbital apex. After
327 being freed from its orbital attachments, the eyeballs were removed from the orbital cavity. A 360-
328 degree concentric limbal incision allowed the removal of cornea, iris, and the lens. Following this
329 procedure, eyeballs were transported to the laboratory in a custom-designed container under
330 continuous oxygenation as described previously (*22*).
331 Exclusion criteria were the presence of significant posterior pole ocular pathology such as age-
332 related macular degeneration, glaucoma, or other retinopathies or optic neuropathies.
333
334 *Brain histopathology*
335 The tissue blocks were embedded in paraffin and 12 µm-thick adjacent sections were stained with
336 hematoxylin-eosin or with antibodies against tau (AT8; Pierce Biotechnology, Rockford, IL, USA,
337 1:1,000, that recognizes the Ser202 and Thr205 epitopes) and Aβ (4G8, Signet Laboratories,
338 Dedham, MA, USA, 1:2,000, that recognizes amino acids 18–22 of the Aβ protein). The
339 neuropathological assessment of Alzheimer disease pathological changes was performed
340 following NIA-AA guidelines(*62*). The severity of tau--immunoreactive lesions, amyloid
341 deposition and neuritic plaques was determined using the Braak stages, Thal phases, and CERAD
342 classification(*20*, *21*, *63*).
343
344 *Retina sampling*

345 The vitreous was removed from the eyecup under dim red light. The macula was identified
346 according to its pigmentation and the pattern of blood vessels in the retina. Circular patches (3 mm
347 diameter) of retina were punched out in an annular region comprised within ~2 to 10 mm from the
348 fovea (except in the blind spot) and from both left and right eyes. Given the number of challenges,
349 including punching out adequate patches, vitreous removal, patches adhesion on the MEA, length
350 of dark adaptation periods and protocol, sampling was done indifferently of the quadrant
351 orientation. While orientation difference may be a source of variability, it seemed a reasonable
352 compromise as this region is relatively homogenous regarding ipRGC density.
353 Samples used for histological experiments were taken in the same region at the end of the recording
354 session and immediately drop in 4% paraformaldehyde (PFA).
355
356 *Retina histopathology*
357 Retinas were fixed in 4% PFA at 4°C for 24 hours, followed by paraffin embedding. Sagittal-
358 oriented sections of the posterior segment were sliced at 10µm thickness. These paraffin sections
359 were treated with 70% formic acid (Roth, 5355.1) for 10 minutes at room temperature, followed
360 by antigen retrieval in citrate buffer (pH 6.0, Merck, 100244) at 100 °C for 1 hour. Sections were
361 then incubated in a blocking solution containing 5% normal goat serum (Sigma, D9663) and 0.05%
362 Triton X-100 (Sigma, T9284) in Tris-buffered saline (TBS; Sigma, 94158) at room temperature
363 for 1 hour. Then, sections were incubated overnight at 4 °C with primary antibodies: anti-Amyloid
364 Beta (ABeta x-42, clone 12F4, mouse, Merck, 05-831-I, 1:500) or anti-Tau (AT8, p-tau
365 Ser202/Thr205, mouse, ThermoFisher, MN1020, 1:250), diluted in 2% blocking buffer. Sections
366 were washed with TBS containing 0.05% Triton X-100, followed by incubation with secondary
367 antibodies (anti-mouse Alexa Fluor® 488, ThermoFisher, A11029, 1:1000) and counterstaining
368 of nuclei with 4′,6-diamidino-2-phenylindole (DAPI; Sigma, D9542) for 3 hours at room
369 temperature. Finally, sections were mounted with Inova Mounting Medium (Ruwag Handels AG,
370 508005). Images were acquired at 40x magnification using a scanning laser microscope (Nikon,
371 Eclipse 80i). Three to six distinct sections imaged per donor. Controls were processed using
372 identical protocols while omitting primary antibody to assess non-specific labelling. The outer and
373 inner retinas, including respectively the photoreceptor and outer plexiform layers and the inner
374 nuclear layer, inner plexiform layer and RGCs layer, were manually segmented using Fiji software

375 (NIH). The average intensity of the aggregates fluorescent signal and the thickness of these regions
376 were measured.
377
378 *Melanopsin Immunofluorescence*
379 Immunohistochemistry was performed as described in detail previously(*25*, *64*). The flat-mount
380 pieces of retinas were incubated in 5% normal donkey serum for 20 min to avoid nonspecific
381 staining. The flat-mount was incubated for 3–4 days with melanopsin primary antibody at 4°C.
382 The patches were then washed and incubated with secondary antibodies for 2 to 3hours at room
383 temperature. Control experiments were performed by eliminating the primary antibody, which
384 abolished all specific staining. Experimenters blinded for the donor ID and pathology were asked
385 to count all cells in the pieces of retina and to trace four representative cells in each patches using
386 semi-automated tracing (pluggin SNT in Fiji).
387
388 *Multi-electrode array recordings*
389 Patches of retina were dark incubated in oxygenated Ames solution until recording (at least
390 60min). Retinal patches were mounted on MEA (256 electrodes arranged in a 16 × 16 square grid,
391 Multichannel Systems, Reutlingen, Germany), ganglion cell side contacting the electrodes, and
392 perfused with oxygenated Ames' medium (Sigma-Aldrich, A1420-10X1L) at 34°C. The
393 MEA2100 amplifier was enclosed in a lightproof box located in a room kept in dark with light
394 emitted only from the controller computer screen with red filter on the screen. ipRGC recordings
395 were done in presence of synaptic blockers (CNQX 20µM, L-AP4 20µM, and D-AP5 50µM) and
396 9-cis retinaldehyde. Stock solutions of 9-cis-Retinal (R5754; Sigma–Aldrich) in ethanol (100 mM)
397 were prepared in darkness and stored at −80°C. On the day of the experiment, an aliquot was
398 thawed and diluted to a final concentration of 100 µM in Ames' medium.
399 Data collection, and analysis were performed as previously described(*16*, *22*, *65*). Briefly, the
400 signal was acquired at 10 kHz and filtered using a low pass (<500Hz) and a high pass (>300Hz)
401 filters for the mERGs and for the RGC multiunit spike responses respectively. Thresholds for spike
402 detection were set at 5 times the standard deviation of the noise on each channel. Spike cutouts,
403 consisting of 1 msec preceding and 2 msec after a suprathreshold event, along were sorted into
404 trains of a single cell after recording using Offline Sorter (Plexon, Denton, TX). Data analysis and
405 display were performed using Neuroexplorer (Plexon) and custom software written in MATLAB.

406

407 *Light stimulations*

408 To elicit the mERGs, we used sequences of five 10ms monochromatic light pulses (470nm)
409 separated by 10s of darkness at four increasing irradiances (6.10^9, 7.10^{10}, 2.10^{12}, and 2.10^{13}
410 photons/cm^2/s). To generate ipRGC responses, we applied a protocol consisting in a sequence of
411 four 30s light stimulations of increasing irradiance of light (7.10^{10}, 2.10^{12}, 2.10^{13}, 1.10^{14}, and 1.10^{15}
412 photons/cm^2/s at 470nm,) separated by 2min of darkness. All light stimuli were generated by high
413 brightness LED, LuxeonStar 5 located ~20cm at the vertical above the MEA. Stimuli were
414 controlled by a homemade C+ program and synchronized to the electrophysiological recordings.
415 The light intensities were measured with a powermeter (PM120D, Thor labs). The ENLIGHT
416 Checklist form will be filled out at the time of publication to show the characteristics of our study
417 and the light used (Supplementary Table XX), as recommended (*66*).

418

419 *ipRGC response parameters analysis*

420 The response discharge rate was calculated as the average of the discharge rate measured during
421 the stimulation (30s) minus the average discharge rate measure during the 30s prior to the
422 stimulation (baseline). The response latency was defined as the delay between the start of the
423 stimulation and the response crossing a threshold set at baseline +2*SD. The response was
424 considered over after firing rate dropped below the baseline level for more than 3 seconds. The
425 dose-response curves (DRCs) were obtained by plotting the response (Y, discharge rate) as a
426 function of the irradiance of the stimulation (X, photon/cm^2/s). DRCs were fitted by a Michaelis-
427 Menten function of the form; Y=Rmax*X/(EC50+X) where Rmax is the maximum response and
428 EC50 is the irradiance required to drive a 50 percent response. A few inhibitory responses were
429 manually discarded.

430

431 *ipRGCs clustering*

432 To distinguish functional types of ipRGCs in the mouse, we performed principal component
433 analysis (PCA) on sensitivity, duration, and latency of the response as previously described(*22*,
434 *67*, *68*). PCA allowed reducing the dimensionality of the data set; the first two principal
435 components accounted for almost 65.5% of the variance (PC1=47.1% and PC2=18.4%). Thus, we
436 next performed k-means clustering analysis on the first two principal components. This model

437 produced clusters that corresponded to the initial analysis. To determine the number of ipRGC
438 clusters, the first two principal components were fitted with Gaussian mixture models (GMMs).
439 We produced separate GMMs for 1 to 5 ipRGCs clusters and then used the Akaike information
440 criterion (AIC) to determine which GMM reported best the ipRGCs distribution. When we
441 compared the 1 to 5 cluster models, the models with the smallest AIC value (best model) were the
442 3, 4, and 5 clusters model. We represented the 3 clusters model as the minimum number of
443 functional subtypes.
444
445 *Statistical analysis*
446 All data are expressed as means ± SEM unless stated otherwise. GraphPad Prism was used for all
447 statistical analyses. Statistical tests used are stated in the figure's legends. Differences between
448 groups were considered statistically significant for $p<0.05$. Bivariate correlation analysis between
449 histological (ipRGC/mRGC density, morphological parameters, Thal/Braak scores, severity of
450 brain pathology) and clinical data (age, collection delay) was performed using Pearson coefficient.
451 Matlab (2019a) was used for k-means and hierarchical clustering, PCA, GMM, and AIC analysis
452 (Statistics and Machine Learning Toolbox).
453

Table1: Donor's demographic and pathology. Amyloid and tau pathologies were evaluated with Thal phases and Braak stages respectively.

	Age (years)	*Sex*	*Delay to Brain collection (hours)*	*Delay to Eyes collection (hours)*	*Cause of death*	*Thal βAmyloid (A)*	*Braak NFT (B)*	*CERAD (C)*	*CAA*	*Brain histology*	*Retina histology*	*Retina function*	*Figure symbols*
D1	71	M	6	2	Brain infarct, hemorrhage	0 (0)	II (1)	0	+	X	x	x	●
D2	80	F	25	2	Brain infarct	2 (1)	III (2)	2	-	X	x	x	■
D3	77	M	13	2	Brain hemorrhage	4 (3)	VI (3)	3	+	X	x	x	▲
D4	85	M	34	2	Brain hemorrhage	2 (3)	I (1)	0	+	X			
D5	89	F	114	1.5	Brain infarct	3 (2)	V (3)	2	+	X	x	x	▼
D6	97	M	27	9	Brain infarct	4 (3)	II (1)	0	+	X			
D7	103	F	3	1	Brain infarct	1 (1)	II (1)	0	-	X			
D8	74	M	11	0.5	Brain infarct	1 (1)	II (1)	0	-	X	x	x	○
D9	74	M	46	2	Brain infarct	0 (0)	I (1)	0	-	X			
D10	70	F	82	82	Brain hemorrhage	0 (0)	II (1)	0	-	X			
D11	77	M	41	2	Brain hemorrhage	2(1)	II (1)	0	-	X	x		♦
D12	69	M	20	2	Brain infarct	0 (0)	I (1)	0	-	X			
D13	91	M	18	2	Brain hemorrhage	2 (1)	0 (0)	0	-	X	x	x	□

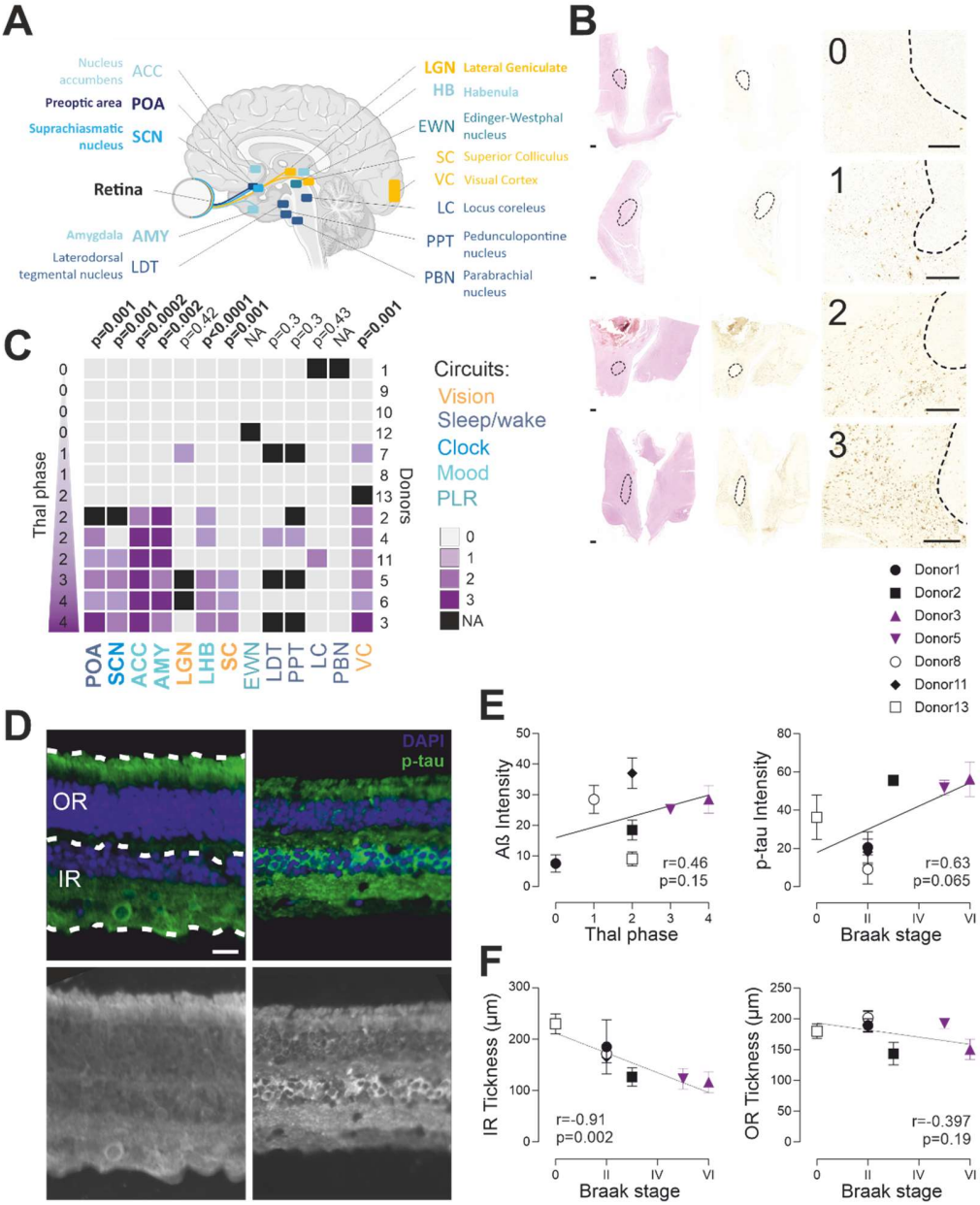

Figure 1: AD hallmarks are present along the circuit of light perception. (**A**) Several brain nuclei contributing to the main light-regulated function (vision, entrainment of the circadian clock, PLR, sleep/alertness, mood) were collected. (**B**) Hypothalamic region including POA from 4 donors exhibiting increasing levels of Aβ deposits (scored 1 to 4). *Left, middle, and right columns,* H&E staining, Aβ staining, and related enlargement respectively (*dotted lines*, fornix; scale bars, 1mm). (**C**) Aβ deposits scores for each brain nuclei in each donor ranked as a function of their

Thal phase. (**D**) Fluorescence micrographs of retinal cross-sections from donor 7 (ND, left column) and donor 3 (AD, right column) with Thal phases 2 and 5 and Braak scores II and VI respectively. On the upper left panel, dotted lines materialized the definition of the Outer and Inner retinas (OR and IR). (*Upper row*) Tissues were immunolabeled for p-tau (AT8, green), and DAPI+-nuclei (blue;). Scale bar: 50 µm. (*Lower row*) Greyscale micrographs the same individuals immunolabeled with p-tau (Scale bar: 50 µm). Scatter plots of the thickness of the donors' IR (**E**) and OR (**F**) as a function of their Braak score (n= 3 to 9 sections measured, Pearson correlation coefficient and p value). Scatter plots of the Aβ (**G**) and p-tau (**H**) burdens measured in each donors as a function of the Thal phase and Braak scores of the donors respectively (n=3 to 5 for Aβ and n=3 for Tau per donor, Pearson correlation coefficient and p value).

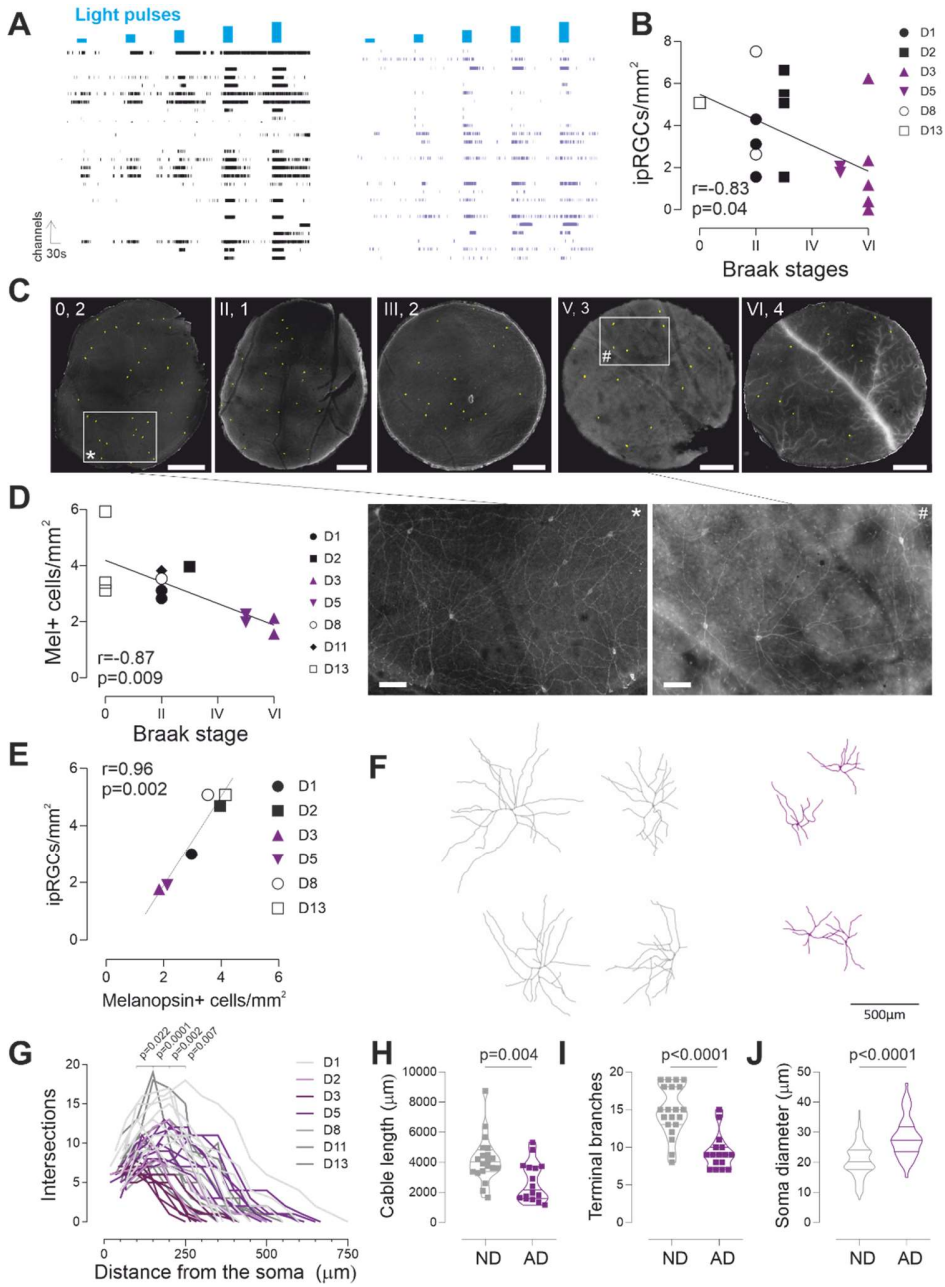

Figure 2: ipRGCs decline in AD. (A) Representative ipRGC spike trains to a 30-s light pulses of increasing irradiance (~1010 to 1015 photons/cm2/s, 470 nm) from AD and age-matched ND donors. (**B**) ipRGCs density in pieces of retina from each donor as a function of their Braak score (n=1 to 5 retina pieces per donor). (**C**, *Upper row*) Microphotographs of patches of retina immunostained against melanopsin (scale bar 500µm, *upper right corner*, Braak stage and Thal phase of the donors). (*Lower row*) Enlargements from the first (*) and fourth (#) patch

487 microphotographs (scale bar 100µm). The mel+ cells density in each donor correlates with their
488 Braak score (**D**, n=1 to 2 retina pieces per donor) and with the density of ipRGCs reported in the
489 same donors (**E**). (**F**) Examples of dendritic shrinkage, mel+ cells from AD (Donor3, *purple*) and
490 age-matched (Donor1, *grey*) donors (scale bar 500µm). Scholl analysis (**G**), neurites length (**H**),
491 number of terminal branches (**I**), and soma diameter (**J**) from AD (n=8 cells per donor, 2 donors,
492 *purple*) and age-matched (n= 4 to 8 cells per donor, 4 donors, *grey*) donors were different.
493

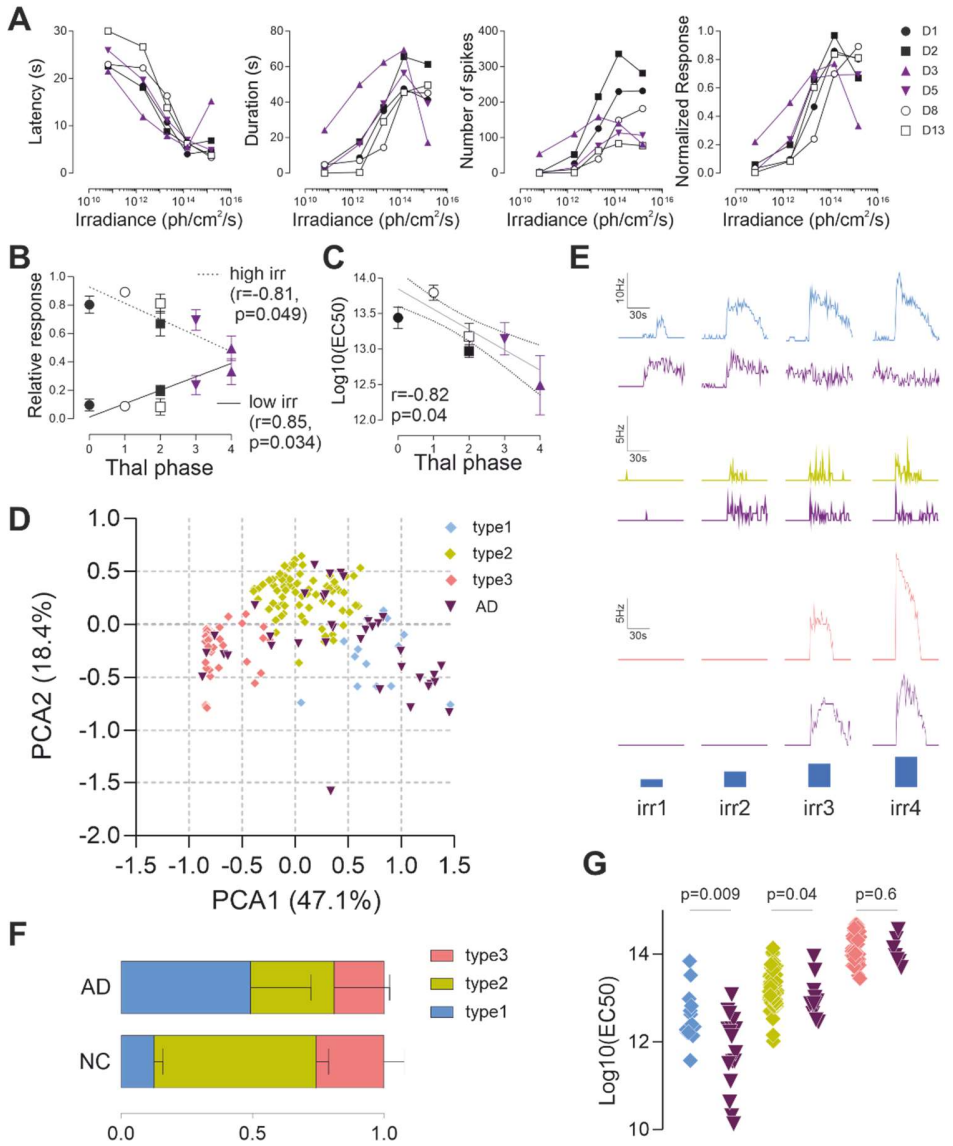

Figure 3: ipRGC function is altered in AD. (**A**) Average ipRGCs'response latency, duration, number of spikes, and normalized response in each donor (n=28, 15, 18, 19, 77, and 13 for donors 1, 2, 3, 5, 8, and 13 respectively, where n is the number of cells) to a sequence of 30s light pulses of increasing irradiance (~10^{10} to 10^{15} photons/cm^2/s, 470 nm). (**B**) Responses to low and high light stimulations as a function of donors' Thal phase ($2x10^{12}$ and $1.5x10^{15}$ photons/cm^2/s, respectively). (**D**) Average ipRGC sensitivity to light as a function of Thal phase. (**E**) Representative responses from types 1, 2, and 3 ipRGCs to increasing irradiance light pulses (30 s, 470 nm, irradiances (irr) 1, 2, 3, and 4: $2x10^{12}$, $2x10^{13}$, $1.5x10^{14}$, and $1.5x10^{15}$ photons/cm^2/s, respectively). Blue bars indicate light pulses. (**F**) Principal components of the ipRGCs' response

505 parameters (sensitivity, latency, and duration; n =133 and n=37, four control and two AD donors
506 (*purple*) respectively). (**G**) Distribution of ipRGC subtypes in ND and AD donors. (**H**) ipRGC
507 sensitivity by subtype in NC and AD donors (n=14, 77, and 45, type1, 2, and 3 cells and n=7, 12,
508 and 18 type1, 2, and 3 cells respectively).
509

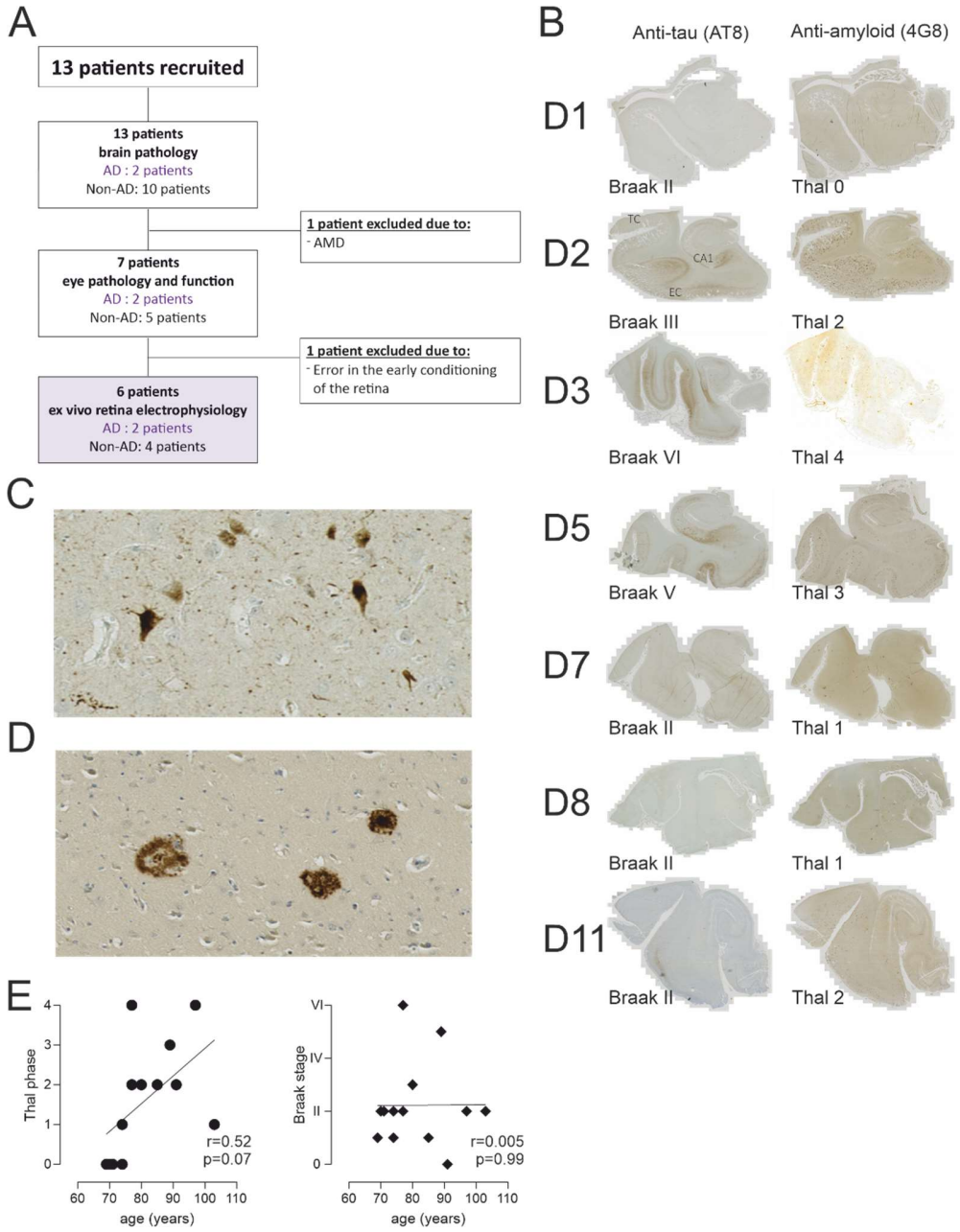

Supplemental Figure 1: Donor's inclusion and neuropathology. (**A**) Donor inclusion flow chart. 13 brain-eye donors were included in our protocol in 2021 and 2022 of which two had to be excluded; one due to AMD diagnostic and a second following an error in eye conditioning. 7 pair of eyes were collected within 2h and could be recorded on MEA. (**B**) NFT and Aβ deposition in the hippocampal formation and the temporal neocortex (CA1 sector of the hippocampus; EC = entorhinal cortex; TC = temporal cortex). Left column: anti-tau (AT8); right column: anti amyloid

518 (4G8) immunostaining. High magnification of neurofibrillary tangle (**C**) and cored senile plaque
519 (**D**) (C: AT8 tau immunohistochemistry; D: 4G8 amyloid immunohistochemistry. (**E**) Neither the
520 Thal phase nor the Braak stage were correlated with the age of the donors.
521

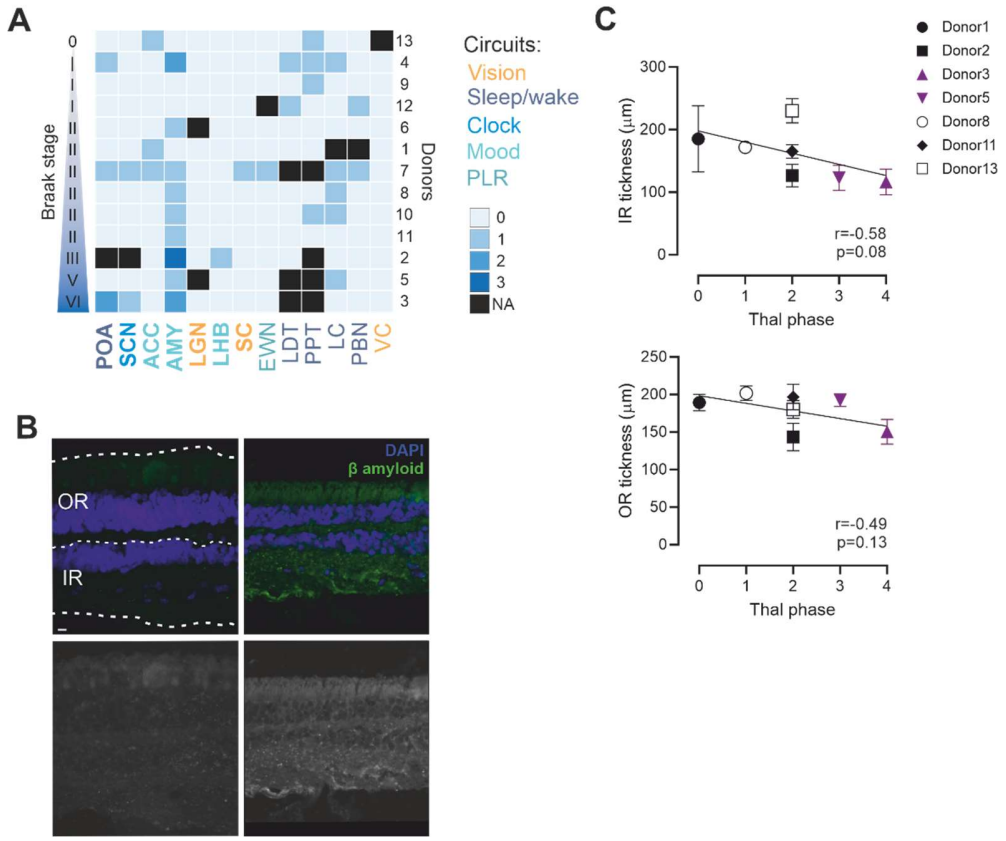

Supplemental Figure 2: AD hallmarks in the brain and in the retina. (**A**) Heatmap of the tau deposits scores for each brain nuclei in each donors ranked as a function of their Braak score. (**B**) Fluorescence micrographs of retinal cross-sections from donors 7 (left column) and 3 (right column) with Thal phases 2 and 5 and Braak stages II and VI respectively. On the upper left panel, dotted lines materialized the definition of the Outer and Inner retinas (OR and IR). (*Upper row*) Tissues were immunolabeled for 12F4+-Aβ42 (green), and DAPI+-nuclei (blue;). Scale bar: 50 µm. (*Lower row*) Greyscale micrographs the same individuals immunolabeled with 12F4+-Aβ42. (**C**) Correlation of outer and inner retina thickness with the Thal phase of the donors.

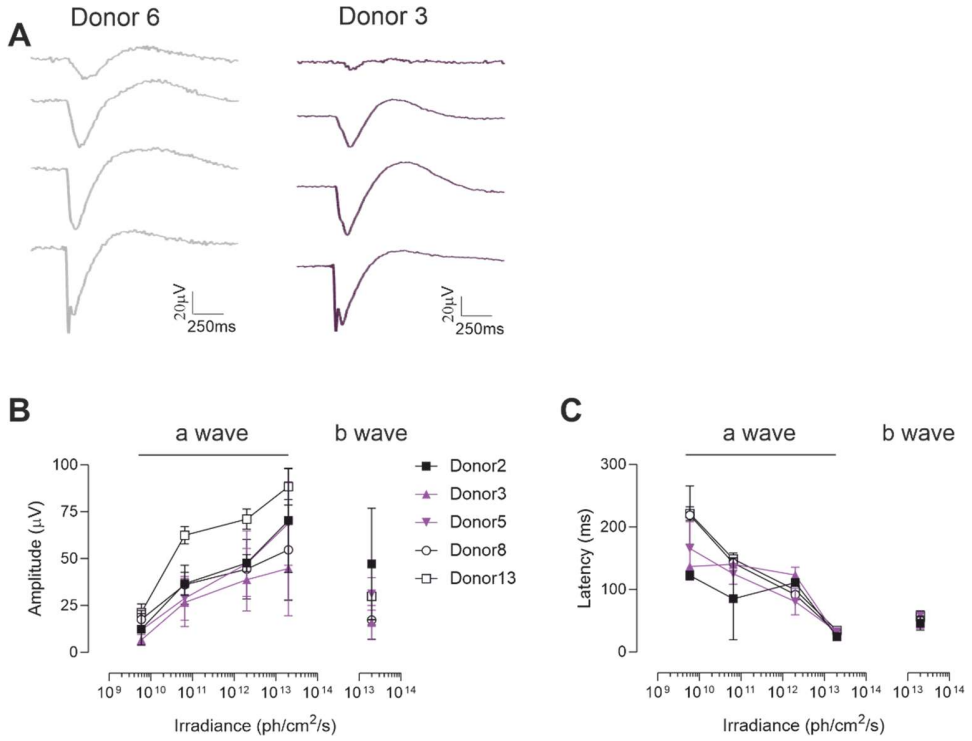

Supplemental Figure 3: ipRGC abundancy and morphology decline in AD. (**A**) ipRGC density do not correlate with either the Thal phase, age of the donor, or delay of eye collection. (**B**) Comparison of density of mel+ cells and ipRGCs measured in patches of retina from ND and AD donors. (**C**) Correlation of each mel+ cell measurement (neurites length, number of nodes, and soma diameter) with Thal phases and Braak stages of the donors (*upper* and *lower* rows respectively).

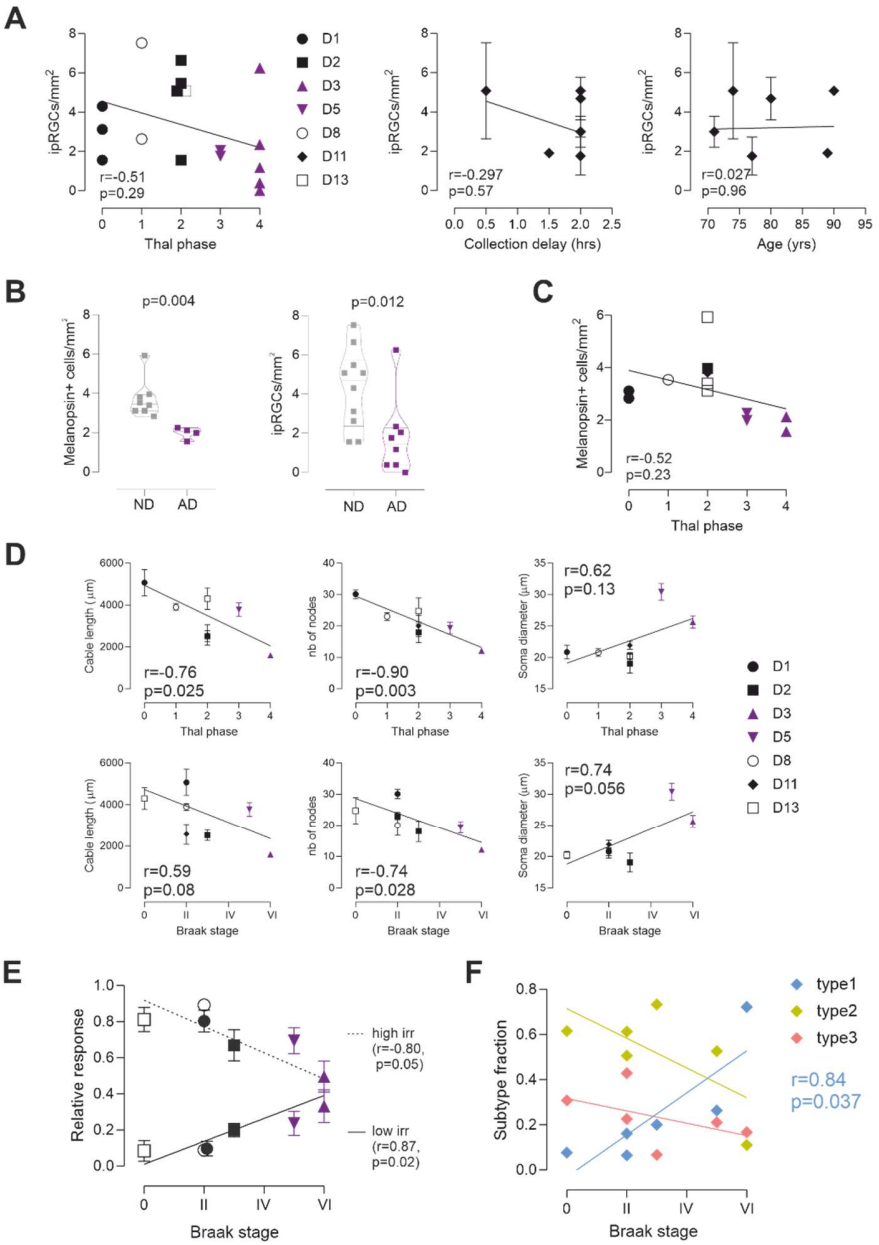

Supplemental Figure 4: *ex vivo* micro Electroretinogram (mERG). (**A**) Representative mERG traces from AD and age-matched donor in response to 10ms light pulses of increasing irradiance (6.10^9, 7.10^{10}, 2.10^{12}, and 2.10^{13} photons/cm^2/s, 470nm) (average of n=247 and n=244 mERG respectively). Dose response curves reporting the average amplitude (**B**) and latency (**C**) of the a and b waves in donors 2, 3, 5, 8, and 13 in response to 10ms light pulses of increasing irradiance (6.10^9, 7.10^{10}, 2.10^{12}, and 2.10^{13} photons/cm^2/s, 470nm) (n=2, 3, 3, 2, and 3 retina pieces in donors 2, 3, 5, 8, and 13 respectively). (**D**) ipRGC subtypes distribution as a function of Braak stage.

References

1. P. Scheltens, K. Blennow, M. M. B. Breteler, B. de Strooper, G. B. Frisoni, S. Salloway, W. M. Van der Flier, Alzheimer's disease. *The Lancet* **388**, 505–517 (2016).

2. E. Nichols, J. D. Steinmetz, S. E. Vollset, K. Fukutaki, J. Chalek, F. Abd-Allah, A. Abdoli, A. Abualhasan, E. Abu-Gharbieh, T. T. Akram, H. A. Hamad, F. Alahdab, F. M. Alanezi, V. Alipour, S. Almustanyir, H. Amu, I. Ansari, J. Arabloo, T. Ashraf, T. Astell-Burt, G. Ayano, J. L. Ayuso-Mateos, A. A. Baig, A. Barnett, A. Barrow, B. T. Baune, Y. Béjot, W. M. M. Bezabhe, Y. M. Bezabih, A. S. Bhagavathula, S. Bhaskar, K. Bhattacharyya, A. Bijani, A. Biswas, S. R. Bolla, A. Boloor, C. Brayne, H. Brenner, K. Burkart, R. A. Burns, L. A. Cámera, C. Cao, F. Carvalho, L. F. S. Castro-de-Araujo, F. Catalá-López, E. Cerin, P. P. Chavan, N. Cherbuin, D.-T. Chu, V. M. Costa, R. A. S. Couto, O. Dadras, X. Dai, L. Dandona, R. Dandona, V. D. la Cruz-Góngora, D. Dhamnetiya, D. D. da Silva, D. Diaz, A. Douiri, D. Edvardsson, M. Ekholuenetale, I. E. Sayed, S. I. El-Jaafary, K. Eskandari, S. Eskandarieh, S. Esmaeilnejad, J. Fares, A. Faro, U. Farooque, V. L. Feigin, X. Feng, S.-M. Fereshtehnejad, E. Fernandes, P. Ferrara, I. Filip, H. Fillit, F. Fischer, S. Gaidhane, L. Galluzzo, A. Ghashghaee, N. Ghith, A. Gialluisi, S. A. Gilani, I.-R. Glavan, E. V. Gnedovskaya, M. Golechha, R. Gupta, V. B. Gupta, V. K. Gupta, M. R. Haider, B. J. Hall, S. Hamidi, A. Hanif, G. J. Hankey, S. Haque, R. K. Hartono, A. I. Hasaballah, M. T. Hasan, A. Hassan, S. I. Hay, K. Hayat, M. I. Hegazy, G. Heidari, R. Heidari-Soureshjani, C. Herteliu, M. Househ, R. Hussain, B.-F. Hwang, L. Iacoviello, I. Iavicoli, O. S. Ilesanmi, I. M. Ilic, M. D. Ilic, S. S. N. Irvani, H. Iso, M. Iwagami, R. Jabbarinejad, L. Jacob, V. Jain, S. K. Jayapal, R. Jayawardena, R. P. Jha, J. B. Jonas, N. Joseph, R. Kalani, A. Kandel, H. Kandel, A. Karch, A. S. Kasa, G. M. Kassie, P. Keshavarz, M. A. Khan, M. N. Khatib, T. A. M. Khoja, J. Khubchandani, M. S. Kim, Y. J. Kim, A. Kisa, S. Kisa, M. Kivimäki, W. J. Koroshetz, A. Koyanagi, G. A. Kumar, M. Kumar, H. M. Lak, M. Leonardi, B. Li, S. S. Lim, X. Liu, Y. Liu, G. Logroscino, S. Lorkowski, G. Lucchetti, R. L. Saute, F. G. Magnani, A. A. Malik, J. Massano, M. M. Mehndiratta, R. G. Menezes, A. Meretoja, B. Mohajer, N. M. Ibrahim, Y. Mohammad, A. Mohammed, A. H. Mokdad, S. Mondello, M. A. A. Moni, M. Moniruzzaman, T. B. Mossie, G. Nagel, M. Naveed, V. C. Nayak, S. N. Kandel, T. H. Nguyen, B. Oancea, N. Otstavnov, S. S. Otstavnov, M. O. Owolabi, S. Panda-Jonas, F. P. Kan, M. Pasovic, U. K. Patel, M. Pathak, M. F. P. Peres, A. Perianayagam, C. B. Peterson, M. R. Phillips, M. Pinheiro, M. A. Piradov, C. D. Pond, M. H. Potashman, F. H. Pottoo, S. I. Prada, A. Radfar, A. Raggi, F. Rahim, M. Rahman, P. Ram, P. Ranasinghe, D. L. Rawaf, S. Rawaf, N. Rezaei, A. Rezapour, S. R. Robinson, M. Romoli, G. Roshandel, R. Sahathevan, A. Sahebkar, M. A. Sahraian, B. Sathian, D. Sattin, M. Sawhney, M. Saylan, S. Schiavolin, A. Seylani, F. Sha, M. A. Shaikh, K. S. Shaji, M. Shannawaz, J. K. Shetty, M. Shigematsu, J. I. Shin, R. Shiri, D. A. S. Silva, J. P. Silva, R. Silva, J. A. Singh, V. Y. Skryabin, A. A. Skryabina, A. E. Smith, S. Soshnikov, E. E. Spurlock, D. J. Stein, J. Sun, R. Tabarés-Seisdedos, B. Thakur, B. Timalsina, M. R. Tovani-Palone, B. X. Tran, G. W. Tsegaye, S. V. Tahbaz, P. R. Valdez, N. Venketasubramanian, V. Vlassov, G. T. Vu, L. G. Vu, Y.-P. Wang, A. Wimo, A. S. Winkler, L. Yadav, S. H. Y. Jabbari, K. Yamagishi, L. Yang, Y. Yano, N. Yonemoto, C. Yu, I. Yunusa, S. Zadey, M. S. Zastrozhin, A. Zastrozhina, Z.-J. Zhang, C. J. L. Murray, T. Vos, Estimation of the global prevalence of dementia in 2019 and forecasted prevalence in 2050: an analysis for the Global Burden of Disease Study 2019. *The Lancet Public Health* **7**, e105–e125 (2022).

3. D. A. Weldemichael, G. T. Grossberg, Circadian Rhythm Disturbances in Patients with Alzheimer's Disease: A Review. *International Journal of Alzheimer’s Disease* **2010**, e716453 (2010).

4. E. J. van Someren, E. E. Hagebeuk, C. Lijzenga, P. Scheltens, S. E. de Rooij, C. Jonker, A. M. Pot, M. Mirmiran, D. F. Swaab, Circadian rest-activity rhythm disturbances in Alzheimer's disease. *Biol Psychiatry* **40**, 259–270 (1996).

596 5. Y.-H. Wu, D. F. Swaab, Disturbance and strategies for reactivation of the circadian rhythm system
597 in aging and Alzheimer's disease. *Sleep Medicine* **8**, 623–636 (2007).

598 6. M. S. Uddin, D. Tewari, A. A. Mamun, M. T. Kabir, K. Niaz, M. I. I. Wahed, G. E. Barreto, G. M.
599 Ashraf, Circadian and sleep dysfunction in Alzheimer's disease. *Ageing Res Rev* **60**, 101046 (2020).

600 7. A. Videnovic, A. S. Lazar, R. A. Barker, S. Overeem, 'The clocks that time us'--circadian rhythms in
601 neurodegenerative disorders. *Nat Rev Neurol* **10**, 683–693 (2014).

602 8. E. S. Musiek, M. Bhimasani, M. A. Zangrilli, J. C. Morris, D. M. Holtzman, Y.-E. S. Ju, Circadian Rest-
603 Activity Pattern Changes in Aging and Preclinical Alzheimer Disease. *JAMA Neurol*, doi:
604 10.1001/jamaneurol.2017.4719 (2018).

605 9. A. Tsapanou, Y. Gu, J. Manly, N. Schupf, M.-X. Tang, M. Zimmerman, N. Scarmeas, Y. Stern,
606 Daytime Sleepiness and Sleep Inadequacy as Risk Factors for Dementia. *DEE* **5**, 286–295 (2015).

607 10. E. A. Hahn, H.-X. Wang, R. Andel, L. Fratiglioni, A Change in Sleep Pattern May Predict Alzheimer
608 Disease. *The American Journal of Geriatric Psychiatry* **22**, 1262–1271 (2014).

609 11. R. Sterniczuk, O. Theou, B. Rusak, K. Rockwood, Sleep Disturbance is Associated with Incident
610 Dementia and Mortality. *Current Alzheimer Research* **10**, 767–775.

611 12. E. S. Musiek, D. D. Xiong, D. M. Holtzman, Sleep, circadian rhythms, and the pathogenesis of
612 Alzheimer Disease. *Exp Mol Med* **47**, e148 (2015).

613 13. A. D. Güler, J. L. Ecker, G. S. Lall, S. Haq, C. M. Altimus, H.-W. Liao, A. R. Barnard, H. Cahill, T. C.
614 Badea, H. Zhao, M. W. Hankins, D. M. Berson, R. J. Lucas, K.-W. Yau, S. Hattar, Melanopsin cells are
615 the principal conduits for rod-cone input to non-image-forming vision. *Nature* **453**, 102–105
616 (2008).

617 14. M. Hatori, H. Le, C. Vollmers, S. R. Keding, N. Tanaka, T. Buch, A. Waisman, C. Schmedt, T. Jegla, S.
618 Panda, Inducible ablation of melanopsin-expressing retinal ganglion cells reveals their central role
619 in non-image forming visual responses. *PLoS ONE* **3**, e2451 (2008).

620 15. C. M. Altimus, A. D. Güler, K. L. Villa, D. S. McNeill, T. A. Legates, S. Hattar, Rods-cones and
621 melanopsin detect light and dark to modulate sleep independent of image formation. *Proc. Natl.*
622 *Acad. Sci. U.S.A* **105**, 19998–20003 (2008).

623 16. L. S. Mure, M. Hatori, Q. Zhu, J. Demas, I. M. Kim, S. K. Nayak, S. Panda, Melanopsin-Encoded
624 Response Properties of Intrinsically Photosensitive Retinal Ganglion Cells. *Neuron* **90**, 1016–1027
625 (2016).

626 17. C. L. Morgia, F. N. Ross-Cisneros, Y. Koronyo, J. Hannibal, R. Gallassi, G. Cantalupo, L. Sambati, B. X.
627 Pan, K. R. Tozer, P. Barboni, F. Provini, P. Avanzini, M. Carbonelli, A. Pelosi, H. Chui, R. Liguori, A.
628 Baruzzi, M. Koronyo-Hamaoui, A. A. Sadun, V. Carelli, Melanopsin retinal ganglion cell loss in
629 Alzheimer disease. *Annals of Neurology* **79**, 90–109 (2016).

630 18. L. Carrero, D. Antequera, I. Alcalde, D. Megías, J. Figueiro-Silva, J. Merayo-Lloves, C. Municio, E.
631 Carro, Disturbed circadian rhythm and retinal degeneration in a mouse model of Alzheimer's
632 disease. *Acta Neuropathologica Communications* **11**, 55 (2023).

633 19. T. K. Weigel, C. L. Guo, A. D. Güler, H. A. Ferris, Altered circadian behavior and light sensing in
634 mouse models of Alzheimer's disease. *Frontiers in Aging Neuroscience* **15** (2023).

635 20. H. Braak, E. Braak, Neuropathological stageing of Alzheimer-related changes. *Acta Neuropathol* **82**,
636 239–259 (1991).

637 21. D. R. Thal, U. Rüb, M. Orantes, H. Braak, Phases of A beta-deposition in the human brain and its
638 relevance for the development of AD. *Neurology* **58**, 1791–1800 (2002).

639 22. L. S. Mure, F. Vinberg, A. Hanneken, S. Panda, Functional diversity of human intrinsically
640 photosensitive retinal ganglion cells. *Science* **366**, 1251–1255 (2019).

641 23. F. Abbas, S. Becker, B. W. Jones, L. S. Mure, S. Panda, A. Hanneken, F. Vinberg, Revival of light
642 signalling in the postmortem mouse and human retina. *Nature*, 1–7 (2022).

643 24. M. Fujii, G. A. Sunagawa, M. Kondo, M. Takahashi, M. Mandai, Evaluation of micro
644 Electroretinograms Recorded with Multiple Electrode Array to Assess Focal Retinal Function. *Sci*
645 *Rep* **6**, 30719 (2016).

646 25. J. Hannibal, A. T. Christiansen, S. Heegaard, J. Fahrenkrug, J. F. Kiilgaard, Melanopsin expressing
647 human retinal ganglion cells: Subtypes, distribution, and intraretinal connectivity. *Journal of*
648 *Comparative Neurology* **525**, 1934–1961 (2017).

649 26. H.-W. Liao, X. Ren, B. B. Peterson, D. W. Marshak, K.-W. Yau, P. D. Gamlin, D. M. Dacey,
650 Melanopsin-expressing ganglion cells on macaque and human retinas form two morphologically
651 distinct populations. *J. Comp. Neurol.* **524**, 2845–2872 (2016).

652 27. G. Esquiva, P. Lax, J. J. Pérez-Santonja, J. M. García-Fernández, N. Cuenca, Loss of Melanopsin-
653 Expressing Ganglion Cell Subtypes and Dendritic Degeneration in the Aging Human Retina. *Front*
654 *Aging Neurosci* **9** (2017).

655 28. S. Nasir-Ahmad, S. C. S. Lee, P. R. Martin, U. Grünert, Melanopsin-expressing ganglion cells in
656 human retina: Morphology, distribution, and synaptic connections. *J. Comp. Neurol.*, doi:
657 10.1002/cne.24176 (2017).

658 29. F. J. Hart de Ruyter, T. H. J. Morrema, J. den Haan, Netherlands Brain Bank, J. W. R. Twisk, J. F. de
659 Boer, P. Scheltens, B. D. C. Boon, D. R. Thal, A. J. Rozemuller, F. D. Verbraak, F. H. Bouwman, J. J. M.
660 Hoozemans, Phosphorylated tau in the retina correlates with tau pathology in the brain in
661 Alzheimer's disease and primary tauopathies. *Acta Neuropathol* **145**, 197–218 (2023).

662 30. C. Schön, N. A. Hoffmann, S. M. Ochs, S. Burgold, S. Filser, S. Steinbach, M. W. Seeliger, T.
663 Arzberger, M. Goedert, H. A. Kretzschmar, B. Schmidt, J. Herms, Long-term in vivo imaging of
664 fibrillar tau in the retina of P301S transgenic mice. *PLoS One* **7**, e53547 (2012).

31. M. Koronyo-Hamaoui, Y. Koronyo, A. V. Ljubimov, C. A. Miller, M. K. Ko, K. L. Black, M. Schwartz, D. L. Farkas, Identification of amyloid plaques in retinas from Alzheimer's patients and noninvasive in vivo optical imaging of retinal plaques in a mouse model. *NeuroImage* **54**, S204–S217 (2011).

32. Y. Koronyo, A. Rentsendorj, N. Mirzaei, G. C. Regis, J. Sheyn, H. Shi, E. Barron, G. Cook-Wiens, A. R. Rodriguez, R. Medeiros, J. A. Paulo, V. B. Gupta, A. A. Kramerov, A. V. Ljubimov, J. E. Van Eyk, S. L. Graham, V. K. Gupta, J. M. Ringman, D. R. Hinton, C. A. Miller, K. L. Black, A. Cattaneo, G. Meli, M. Mirzaei, D.-T. Fuchs, M. Koronyo-Hamaoui, Retinal pathological features and proteome signatures of Alzheimer's disease. *Acta Neuropathol* **145**, 409–438 (2023).

33. C. La Morgia, M. Mitolo, M. Romagnoli, M. Stanzani Maserati, S. Evangelisti, M. De Matteis, S. Capellari, C. Bianchini, C. Testa, G. Vandewalle, A. Santoro, M. Carbonelli, P. D'Agati, M. Filardi, P. Avanzini, P. Barboni, C. Zenesini, F. Baccari, R. Liguori, C. Tonon, R. Lodi, V. Carelli, Multimodal investigation of melanopsin retinal ganglion cells in Alzheimer's disease. *Annals of Clinical and Translational Neurology* **n/a** (2023).

34. N. Mirzaei, H. Shi, M. Oviatt, J. Doustar, A. Rentsendorj, D.-T. Fuchs, J. Sheyn, K. L. Black, Y. Koronyo, M. Koronyo-Hamaoui, Alzheimer's Retinopathy: Seeing Disease in the Eyes. *Front. Neurosci.* **14** (2020).

35. A. Cronin-Golomb, R. Sugiura, S. Corkin, J. H. Growdon, Incomplete achromatopsia in Alzheimer's disease. *Neurobiol Aging* **14**, 471–477 (1993).

36. G. Schlotterer, M. Moscovitch, D. Crapper-McLachlan, Visual processing deficits as assessed by spatial frequency contrast sensitivity and backward masking in normal ageing and Alzheimer's disease. *Brain* **107 (Pt 1)**, 309–325 (1984).

37. A. A. Sadun, M. Borchert, E. DeVita, D. R. Hinton, C. J. Bassi, Assessment of visual impairment in patients with Alzheimer's disease. *Am J Ophthalmol* **104**, 113–120 (1987).

38. G. L. Trick, L. R. Trick, P. Morris, M. Wolf, Visual field loss in senile dementia of the Alzheimer's type. *Neurology* **45**, 68–74 (1995).

39. B. Katz, S. Rimmer, Ophthalmologic manifestations of Alzheimer's disease. *Surv Ophthalmol* **34**, 31–43 (1989).

40. G. L. Trick, M. C. Barris, M. Bickler-Bluth, Abnormal pattern electroretinograms in patients with senile dementia of the Alzheimer type. *Ann Neurol* **26**, 226–231 (1989).

41. V. Parisi, R. Restuccia, F. Fattapposta, C. Mina, M. G. Bucci, F. Pierelli, Morphological and functional retinal impairment in Alzheimer's disease patients. *Clin Neurophysiol* **112**, 1860–1867 (2001).

42. F. Sartucci, D. Borghetti, T. Bocci, L. Murri, P. Orsini, V. Porciatti, N. Origlia, L. Domenici, Dysfunction of the magnocellular stream in Alzheimer's disease evaluated by pattern electroretinograms and visual evoked potentials. *Brain Res Bull* **82**, 169–176 (2010).

43. K. Krasodomska, W. Lubiński, A. Potemkowski, K. Honczarenko, Pattern electroretinogram (PERG) and pattern visual evoked potential (PVEP) in the early stages of Alzheimer's disease. *Doc Ophthalmol* **121**, 111–121 (2010).

44. S. Hattar, M. Kumar, A. Park, P. Tong, J. Tung, K.-W. Yau, D. M. Berson, Central projections of melanopsin-expressing retinal ganglion cells in the mouse. *J. Comp. Neurol* **497**, 326–349 (2006).

45. C. Beier, Z. Zhang, M. Yurgel, S. Hattar, Projections of ipRGCs and conventional RGCs to retinorecipient brain nuclei. *J Comp Neurol*, doi: 10.1002/cne.25061 (2020).

46. I. Cobos, J. J. Palop, Swollen axons impair neuronal circuits in Alzheimer's disease. *Nature* **612**, 218–220 (2022).

47. J. Michaud, I. Plu, J. Parai, A. Bourgault, C. Tanguay, D. Seilhean, J. Woulfe, Ballooned neurons in semi-recent severe traumatic brain injury. *Acta Neuropathologica Communications* **11**, 37 (2023).

48. J. Lowe, D. R. Errington, G. Lennox, I. Pike, I. Spendlove, M. Landon, R. J. Mayer, Ballooned neurons in several neurodegenerative diseases and stroke contain αB crystallin. *Neuropathology and Applied Neurobiology* **18**, 341–350 (1992).

49. S. S. Bassett, D. M. Yousem, C. Cristinzio, I. Kusevic, M. A. Yassa, B. S. Caffo, S. L. Zeger, Familial risk for Alzheimer's disease alters fMRI activation patterns. *Brain* **129**, 1229–1239 (2006).

50. N. Filippini, B. J. MacIntosh, M. G. Hough, G. M. Goodwin, G. B. Frisoni, S. M. Smith, P. M. Matthews, C. F. Beckmann, C. E. Mackay, Distinct patterns of brain activity in young carriers of the *APOE*-ε4 allele. *Proceedings of the National Academy of Sciences* **106**, 7209–7214 (2009).

51. H. Targa Dias Anastacio, N. Matosin, L. Ooi, Neuronal hyperexcitability in Alzheimer's disease: what are the drivers behind this aberrant phenotype? *Transl Psychiatry* **12**, 1–14 (2022).

52. Q. Cui, C. Ren, P. J. Sollars, G. E. Pickard, K.-F. So, THE INJURY RESISTANT ABILITY OF MELANOPSIN-EXPRESSING INTRINSICALLY PHOTOSENSITIVE RETINAL GANGLION CELLS. *Neuroscience* **284**, 845–853 (2015).

53. S. B. Baver, G. E. Pickard, P. J. Sollars, G. E. Pickard, Two types of melanopsin retinal ganglion cell differentially innervate the hypothalamic suprachiasmatic nucleus and the olivary pretectal nucleus. *Eur. J. Neurosci.* **27**, 1763–1770 (2008).

54. A. J. Oh, G. Amore, W. Sultan, S. Asanad, J. C. Park, M. Romagnoli, C. La Morgia, R. Karanjia, M. G. Harrington, A. A. Sadun, Pupillometry evaluation of melanopsin retinal ganglion cell function and sleep-wake activity in pre-symptomatic Alzheimer's disease. *PLoS ONE* **14**, e0226197 (2019).

55. G. P. Van Stavern, L. Bei, Y.-B. Shui, J. Huecker, M. Gordon, Pupillary light reaction in preclinical Alzheimer's disease subjects compared with normal ageing controls. *Br J Ophthalmol* **103**, 971–975 (2019).

56. A. Kawasaki, S. Ouanes, S. V. Crippa, J. Popp, Early-Stage Alzheimer's Disease Does Not Alter Pupil Responses to Colored Light Stimuli. *J. Alzheimers Dis.* **75**, 1273–1282 (2020).

57. M. Romagnoli, M. Stanzani Maserati, M. De Matteis, S. Capellari, M. Carbonelli, G. Amore, G. Cantalupo, C. Zenesini, R. Liguori, A. A. Sadun, V. Carelli, J. C. Park, C. La Morgia, Chromatic Pupillometry Findings in Alzheimer's Disease. *Front. Neurosci.* **14** (2020).

58. P. S. Chougule, R. P. Najjar, M. T. Finkelstein, N. Kandiah, D. Milea, Light-Induced Pupillary Responses in Alzheimer's Disease. *Front Neurol* **10**, 360 (2019).

59. M. Romagnoli, G. Amore, P. Avanzini, V. Carelli, C. La Morgia, Chromatic pupillometry for evaluating melanopsin retinal ganglion cell function in Alzheimer's disease and other neurodegenerative disorders: a review. *Front Psychol* **14**, 1295129 (2023).

60. J. den Haan, T. H. J. Morrema, F. D. Verbraak, J. F. de Boer, P. Scheltens, A. J. Rozemuller, A. A. B. Bergen, F. H. Bouwman, J. J. Hoozemans, Amyloid-beta and phosphorylated tau in post-mortem Alzheimer's disease retinas. *Acta Neuropathologica Communications* **6**, 147 (2018).

61. Y. Koronyo, D. Biggs, E. Barron, D. S. Boyer, J. A. Pearlman, W. J. Au, S. J. Kile, A. Blanco, D.-T. Fuchs, A. Ashfaq, S. Frautschy, G. M. Cole, C. A. Miller, D. R. Hinton, S. R. Verdooner, K. L. Black, M. Koronyo-Hamaoui, Retinal amyloid pathology and proof-of-concept imaging trial in Alzheimer's disease. *JCI Insight* **2**, e93621, 93621 (2017).

62. B. T. Hyman, C. H. Phelps, T. G. Beach, E. H. Bigio, N. J. Cairns, M. C. Carrillo, D. W. Dickson, C. Duyckaerts, M. P. Frosch, E. Masliah, S. S. Mirra, P. T. Nelson, J. A. Schneider, D. R. Thal, B. Thies, J. Q. Trojanowski, H. V. Vinters, T. J. Montine, National Institute on Aging-Alzheimer's Association guidelines for the neuropathologic assessment of Alzheimer's disease. *Alzheimers Dement* **8**, 1–13 (2012).

63. S. S. Mirra, A. Heyman, D. McKeel, S. M. Sumi, B. J. Crain, L. M. Brownlee, F. S. Vogel, J. P. Hughes, G. van Belle, L. Berg, The Consortium to Establish a Registry for Alzheimer's Disease (CERAD). Part II. Standardization of the neuropathologic assessment of Alzheimer's disease. *Neurology* **41**, 479–486 (1991).

64. J. Hannibal, L. Kankipati, C. E. Strang, B. B. Peterson, D. Dacey, P. D. Gamlin, Central projections of intrinsically photosensitive retinal ganglion cells in the macaque monkey. *J. Comp. Neurol.* **522**, 2231–2248 (2014).

65. L. S. Mure, M. Hatori, K. Ruda, G. Benegiamo, J. Demas, S. Panda, Sustained Melanopsin Photoresponse Is Supported by Specific Roles of β-Arrestin 1 and 2 in Deactivation and Regeneration of Photopigment. *Cell Reports* **25**, 2497-2509.e4 (2018).

66. M. Spitschan, L. Kervezee, R. Lok, E. McGlashan, R. P. Najjar, A. E. Allen, M. Andersen, S. Bará, P. Blattner, C. Blume, D. B. Boivin, M.-Á. Bonmatí-Carrión, K. Broszio, T. M. Brown, S. L. Chellappa, J. F. Duffy, T. Eto, E. Flynn-Evans, S. Fotios, V. Gabel, C. Garbazza, G. Glickman, M. C. Gordijn, J. P. Hanifin, L. Hartstein, M. Herf, S. Higuchi, C. J. Hilditch, K. W. Houser, A. Hurlbert, M. K. LeBourgeois, S. Lockley, R. Lucas, C. R. C. Moreno, M. Münch, L. S. Mure, S. Peirson, S. Rahman, V. L. Revell, R. G. Rodriguez, K. Roecklein, A. V. Rukmini, J. Sammarco, N. Santhi, L. J. M. Schlangen, I. Schöllhorn, K. M. Sharkey, D. J. Skene, T. L. Sletten, K. C. H. J. Smolders, O. Stefani, J. E. Stone, P. Teikari, M. Terman, K. T. Quoc, K. Tsubota, L. Udovicic, G. Vandewalle, J. A. Veitch, CélineVetter, L. M. Wu, J. Zauner, J. Zeitzer, ENLIGHT: A consensus checklist for reporting laboratory-based studies on the non-visual effects of light in humans. *eBioMedicine* **98** (2023).

67. A. J. Emanuel, K. Kapur, M. T. H. Do, Biophysical Variation within the M1 Type of Ganglion Cell Photoreceptor. *Cell Rep* **21**, 1048–1062 (2017).

68. D. C. Tu, D. Zhang, J. Demas, E. B. Slutsky, I. Provencio, T. E. Holy, R. N. Van Gelder, Physiologic diversity and development of intrinsically photosensitive retinal ganglion cells. *Neuron* **48**, 987–999 (2005).